# Dalton Transactions

Accepted Manuscript






ROYAL SOCIETY OF CHEMISTRY

www.rsc.org/dalton

Journal Name

ARTICLE

# Earth-abundant NiS Co-catalysts Modified Metal-free mpg-$C_3N_4$/CNTs Nanocomposites for Highly Efficient Visible-Light Photocatalytic $H_2$ Evolution

Received 00th January 20xx,
Accepted 00th January 20xx

DOI: 10.1039/x0xx00000x

www.rsc.org/

Yongming Zhong, Jielin Yuan, Jiuqing Wen, Xin Li,* Yuehua Xu, Wei Liu,* Shengsen Zhang, Yueping Fang*

In the present work, the earth-abundant NiS co-catalysts modified mesoporous graphite-like $C_3N_4$ (mpg-$C_3N_4$)/CNTs nanocomposites were prepared via a two-step strategy: sol-gel method and direct precipitation process. The mpg-$C_3N_4$/CNT/NiS composite photocatalysts was characterized by X-ray diffraction (XRD), transmission electron microscopy (TEM), UV-vis absorption spectra, photoluminescence spectroscopy (PL), photoelectrochemical (PEC) and electrochemical impedance spectra (EIS) experiments. The photocatalytic $H_2$-production activity over the composite catalysts was also evaluated by using an aqueous solution containing triethanolamine under visible light (λ≥ 420 nm). The results showed that the loading of earth-abundant NiS co-catalysts onto metal-free mpg-$C_3N_4$/CNTs nanocomposites can remarkably enhance their photocatalytic $H_2$-production activity. The optimal loading amount of NiS on metal-free mpg-$C_3N_4$/CNTs nanocomposites was about 1 wt%. The as-obtained mpg-$C_3N_4$/CNT/1%NiS ternary composite photocatalyst exhibits the best $H_2$-evolution activity with the highest rate of about 521 μmol·$g^{-1}h^{-1}$ under visible light (λ>420 nm), which is almost 148 times higher than that of pure mpg-$C_3N_4$/CNT sample. The enhanced photocatalytic activity can be mainly attributed to due to the synergistic effect of effectively promoted separation of photo generated electron-hole pairs and enhanced $H_2$-evolution kinetics. The co-loading of nanocarbon materials and earth-abundant co-catalysts onto metal-free mpg-$C_3N_4$ nanocomposites offers great potential for practical applications in photocatalytic $H_2$ evolution under visible light illumination.

## 1. INDUCTION

Nowadays, to effectively meet increasing global energy demands and alleviate the energy crisis, there is an urgent need for large-scale development of advanced sustainable and renewable energies such as solar and wind power, which can serve as cost-effective and environmentally potential alternatives to conventional fossil fuels. Meanwhile, it is well known that hydrogen has long been considered one of the most attractive and most promising clean energy carriers due to its high enthalpy value and benign combustion product (water).[1] Among various facile technologies for hydrogen production, solar water splitting over suspended photocatalysts represents an ideal process for generating clean hydrogen ($H_2$) fuel from renewable resources because it provides one of the best solutions to solve both energy and environmental issues.[2-4] In particular, since Fujishima and Honda first revealed the photoelectrochemical water splitting over a $TiO_2$ electrode in 1972,[5] the photocatalytic hydrogen production using solar energy has attracted more and more attention as a very important research area of research.[6, 7] To date, many kinds of powdered photocatalysts and heterogeneous photocatalytic systems for efficient solar hydrogen production have been exploited, but none of them could satisfy all the requirements for practical solar hydrogen generation, such as low cost, nontoxicity, high visible-light activity and good durability.[7] In order to address these issues and achieve the practical photocatalytic hydrogen production, it is necessary to precisely control of the composition and structure of these existing semiconductor materials through various engineering strategies, besides the development of novel visible-light-driven photocatalysts with high quantum efficiency and good photostability.[7]

In 2009, a cheap and nontoxic metal-free polymeric-like carbon nitride with a graphitic structure (g-$C_3N_4$) was first found to be active in photocatalytic water splitting under visible light illumination by Wang's group.[8] Since then, g-$C_3N_4$ has been extensively applied in the various photocatalytic and photovoltaic fields during the past several years, such as photocatalytic degradation,[9, 10] photocatalytic $H_2$ production,[11-14] photocatalytic $CO_2$ reduction,[7, 15-20] photocatalytic organic synthesis[21, 22] and solar cells[23, 24]. In general, the g-$C_3N_4$ with a narrow indirect band gap of about 2.7 eV, possesses suitable conduction band (CB, at -1.3 V at pH 7) and valence band (VB, at 1.4 V at pH 7) positions for

[a] College of Materials and Energy, South China Agricultural University, Guangzhou 510642, P. R. China. Tel.: +86 20 85280325; fax: +86 20 85282366.
E-mail address: Xinliscau@yahoo.com (X. Li), wlscau@163.com (W. Liu), ypfang@scau.edu.cn (Y. Fang)

† Footnotes relating to the title and/or authors should appear here.
Electronic Supplementary Information (ESI) available: [details of any supplementary information available should be included here]. See DOI: 10.1039/x0xx00000x

photocatalytic hydrogen and oxygen production, respectively.[11-13, 25] However, the pure $C_3N_4$ usually exhibits the insufficient absorbance for visible light, poor electrical conductivity, low specific surface area and fast recombination of photo generated electron-hole pairs, significantly limiting its practical application.[26, 27] To efficiently overcome these limitations, it is crucial to further boost the photocatalytic activity of g-$C_3N_4$ through suitable engineering strategies, such as fabricating different nanostructures,[28-31] doping with metal or nometal elements,[16, 22, 32-34] loading co-catalysts,[18, 35, 36] increasing the specific surface area (or introducing mesoporosity),[37, 38] sensitizing by organic dyes [39-42], creating heterojunctions[43-45] and their combinations[46].

To make the g-$C_3N_4$ more active for heterogeneous photocatalytic $H_2$ evolution, the enhancements in its surface active sites and lifetime of photo-generated electrons are of great significance for improving the surface $H_2$-evolution kinetics during the photocatalytic processes. On the one hand, the surface active sites of g-$C_3N_4$ could be greatly enhanced through loading co-catalysts or constructing mesoporous structures, thus leading to the improved $H_2$-evolution activity. For example, it was demonstrated that the introducing mesoporosity into g-$C_3N_4$ through silica-templated self-polymerization route could enhance its hydrogen production rate by a factor of 10 in the presence of Pt co-catalysts, due to the formation of a mesoporous and crystallized g-$C_3N_4$ framework with high surface area.[38] Furthermore, other Pt-free co-catalysts such as $Ag_2S$,[47] $MoS_2$,[48, 49] $WS_2$,[50] Au,[51] $NiS_x$,[52-55] CoS,[56] $Cu(OH)_2$[36] and $Ni(OH)_2$[35] have also been demonstrated to be capable of remarkably enhancing the photocatalytic $H_2$-evolution rate of g-$C_3N_4$. Especially, Ni-based materials as $H_2$-evolution cocatalysts have received much attention because of their low cost, earth-abundant elements and excellent photocatalytic activity.[7, 57, 58] Recently, Xu and co-workers reported that the photocatalytic $H_2$-evolution activity over the optimal NiS(1.1 wt%)/g-$C_3N_4$ photocatalyst was 253 times higher than the pristine g-$C_3N_4$.[53] In addition, the hybridization of nanocarbon materials (such as the multi-walled carbon nanotubes (CNTs) and graphene) and g-$C_3N_4$ also provides an efficient strategy to boost the photocatalytic $H_2$-evolution rate of g-$C_3N_4$ due to the improved electrical conductivity, promoted charge separation, enhanced light-harvesting capacity and increased reactive sites.[14, 59-61] Generally, the loading of CNTs or graphene could achieve a significant activity enhancement (enhanced about 2-4 times) in the existence or absence of Pt co-catalysts.[14, 62-64] However, to our best knowledge, there is no investigation on the photocatalytic $H_2$-production over the hybrid mpg-$C_3N_4$/CNTs nanocomposites modified by noble-metal free NiS co-catalysts.

Here, for the first time, the hybrid mpg-$C_3N_4$/CNTs nanocomposites were synthesized via a facile template method, and were then loaded by NiS co-catalysts through a simple direct precipitation process. Compared to the hybrid mpg-$C_3N_4$/CNTs nanocomposites, the significantly enhanced visible light photocatalytic $H_2$-production activity could be achieved through the loading of NiS co-catalysts. The effect of NiS loading contents on the photocatalytic hydrogen-evolution activity was investigated and discussed in detail. A possible photocatalytic mechanism was also proposed.

## 2. Experimental section

### 2.1. Syntheses of the mpg-$C_3N_4$/CNT

All chemicals were reagent grade and used without further purification. Multi-walled carbon nanotubes (CNTs; purity, >95%; diameter, 40–60 nm; length, 5–15μm; specific surface area, 40–300 $m^2g^{-1}$ ) prepared by catalytic decomposition of $CH_4$ using $La_2NiO_4$ as a catalyst precursor were provided by Shenzhen Nanoport Co., Ltd. (NPT). Cyanamide was obtained from Aldrich.

The metal-free mpg-$C_3N_4$/CNT hybrid powders were synthesized via a sol-gel method. In a typical synthesis, 0.1 g of CNTs powder (with an optimum content of 6.8 wt% in the mpg-$C_3N_4$/CNT nanocomposites, the detailed data were shown in Table S1 and Figure S1-S5) was dispersed in 5 ml of cyanamide aqueous solution (50%) by sonication for 20 min and then slowly adding 5 ml of silica sol (12 nm) to the same beaker under the condition of stirring. After keeping stirring for 5h in room temperature, the mixture was transferred to 20 ml porcelain crucible and dried for 1h at 60˚C to get jelly-like gel. Then, the samples were calcined at 550˚C in $N_2$ atmosphere for 4h, with the heating rate was 2.3˚C/min. After washing the calcined yellow sample with 100 mL $NH_4HF_2$ solution for 24 h, the $SiO_2$ nanoparticles were removed. Finally, the product was harvested by centrifugation and washed with water and absolute ethanol several times, and dried for 12h at 60˚C in vacuum oven.

### 2.2 Syntheses of the mpg-$C_3N_4$/CNT/NiS

The mpg-$C_3N_4$/CNT/NiS samples were prepared through a simple direct precipitation process. The detailed synthesis parameters are shown in Table 1. Typically, 0.3g mpg-$C_3N_4$/CNT was dispersed in 60 ml of water by sonication for 30 min, and 0.660 mL 0.05M nickel acetate solution was added subsequently. After stirring for 1h, the NiS was to form by the addition of 3.305 mL 0.05M $Na_2S$ solution drop by drop, and the theoretical quality ratio of NiS was 1%.

Table 1 Synthesis parameters of different quality ratio of NiS

| Sample | mpg-$C_3N_4$/CNT/g | 0.05M $Ni(Ac)_2$/mL | 0.05M $Na_2S$/mL |
|---|---|---|---|
| g-$C_3N_4$/CNT/0.5%NiS | 0.3 | 0.330 | 1.650 |
| g-$C_3N_4$/CNT/1% NiS | 0.3 | 0.660 | 3.305 |
| g-$C_3N_4$/CNT/3% NiS | 0.3 | 1.985 | 9.915 |

### 2.3. Material Characterization

The structure and morphology of the as-prepared samples were analyzed by X-ray diffraction (XRD; Rigaku, D/max 2500v/pc), transmission electron microscopy (JEOL-2010 microscope operated at 200 kV). A Shimadzu spectrophotometer (model 2501 PC) equipped with an integrating sphere was used to record the UV-vis diffuse reflectance spectra of the samples. The X-ray photoelectron spectroscopy (XPS) was performed with a VG ESCALAB250 surface analysis system using a monochromatized Al Ka X-ray source (300 W, 5 mA, and 15 kV). The base pressure was about $3\times10^{-9}$ mbar. The shift of the binding energy owing to relative surface charging was corrected using the C 1s level at 284.6 eV as an internal standard. Nitrogen adsorption–desorption isotherms were measured on a Gemini-2360 analyzer (Micromeritics Co., USA) at 77 K. The Brunauer–Emmett–Teller (BET) method was used to determine the specific surface area. The pore-size distributions were derived from the desorption branches of the isotherms using the Barrett-Joyner-Halenda (BJH) method. Transmission electron

microscopy (TEM) images and high-resolution transmission electron microscopy (HRTEM) images, and selected area electron diffraction (SAED) patterns were collected on an F20 S-TWIN electron microscope (Tecnai G2, FEI Co.), at a 200 kV accelerating voltage. The photoluminescence (PL) spectra were measured using a LS 50B (PerkinElmer, Inc., USA) with an excitation wavelength of 363 nm at room temperature.

**2.4. Photocatalytic $H_2$ evolution experiments**

Photocatalytic water splitting was carried out in a LabSolar $H_2$ photocatalytic hydrogen evolution system (Perfectlight, Beijing) including a 300W Xe lamp (PLS-SXE300, Beijing Trusttech). In a typical reaction, 50 mg of mpg-$C_3N_4$/CNT/NiS composite was dispersed in a Pyrex glass reactor containing the solution mixing with 90mL water and 10mL triethanolamine (TEOA). Then, the system was sealed and vacuumized to keep the pressure as -0.1 MPa. Afterwards, a circular cooling water system was turned on and the reactor was irradiated with Xe lamp (300 W) under magnetic stirring. The gases evolved were analyzed on line with a gas chromatograph (GC-7900, TCD, with $N_2$ as carrier gas) after 0.5 h of illumination. The reaction was continued for 3h. A cyclic experiment was carried out to investigate the photocatalytic stability of mpg-$C_3N_4$/CNT/NiS composite. After 3h of the reaction, $H_2$ produced was evacuated, and then for another 3h run.

**2.5. Photoelectrochemical measurement**

A working electrode was prepared as follows: 0.05 g of sample was ground with 2mL absolute ethanol and 20uL 0.25% Nafion solution. 500 μL of the mixture was coated onto a 2×6 $cm^2$ fluorine-doped tin-oxide (FTO) glass by a drop casting method, and then dried in an oven and calcined at 150˚C for 1h in a $N_2$ gas flow to obtain working electrodes. Photocurrents were measured on an electrochemical analyzer ((BAS100 Instruments) in a standard three-electrode system by using the prepared film as the working electrode, a Pt flake as the counter electrode, and Ag/AgCl (saturated KCl) as the reference electrode. A 300 W Xe-lamp served as a light source, and 0.1 M $Na_2SO_4$ solution was used as the electrolyte. The electrochemical impedance spectra (EIS) of above-mentioned working electrodes in the three-electrode system were also recorded via a computer controlled IM6e impedance measurement unit (Zahner Elektrik, Germany) over a frequency range of 0.01–$10^5$ Hz with an ac amplitude of 5 mV, under visible light illumination. 0.5M $Na_2SO_4$ aqueous solutions were used as the electrolyte.

## 3. Results and discussion

**3.1 XRD characterization**

The structure and composition of all mpg-$C_3N_4$/CNT/NiS samples were initially investigated by XRD. Figure 1 shows the XRD patterns of the mpg-$C_3N_4$/CNT samples with different NiS contents. As observed from the XRD patterns in Figure 1, all the samples exhibit a similar rectangular shape with one typical (002) interlayer-stacking diffraction peak at 27.5˚. Clearly, this high-intensity diffraction peak identified in all patterns represents the graphite-like stacking of the conjugated aromatic units in $C_3N_4$ layers, corresponding well to the interlayer d-spacing (0.336 nm) of g-$C_3N_4$.[8] It is also noted that the weakest diffraction peak at 13.04° was also observed, corresponding to (100) peak that arises from the in-plane ordering of tri-s-triazine units (with an interplanar separation of 0.672 nm).[39, 44] In addition, no other noticeable diffraction peaks corresponding to CNTs (an apparent XRD peak at 26.2°)[65] or NiS were detected from XRD pattern of all mpg-$C_3N_4$/CNT/NiS composite samples in Figure 1, which may be presumably attributed to the low contents and highly selective dispersion of the loaded CNTs and/or NiS nanoparticles in the composite samples.[59] It can also be observed from the XRD results that the loading of CNTs and NiS nanoparticles has no significant influence on the structure of mpg-$C_3N_4$, and no additional diffraction peak can be detected.

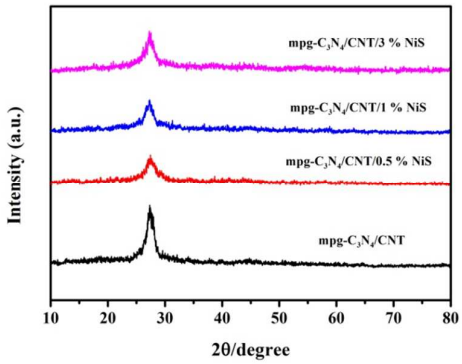


**Figure 1**. XRD patterns of the mpg-$C_3N_4$/CNT samples with different NiS contents.

**3.2 TEM characterization**

The morphology and microstructure of mpg-$C_3N_4$/CNT/NiS samples were further observed by TEM. TEM images of mpg-$C_3N_4$/CNT and mpg-$C_3N_4$/CNT/1% NiS are displayed in Figure 2A and 2B, respectively. As shown in Figure 2A, mpg-$C_3N_4$ exhibits a typical layered platelet-like and porous morphology after the removal of $SiO_2$ templates. Furthermore, the high dispersion of CNTs in the mpg-$C_3N_4$ was achieved, which could lead to the formation of the intimate interactions between CNTs and mpg-$C_3N_4$, thus facilitating effective charge separation and photocatalytic activity enhancements. In addition, it was observed from Figure 2B that many dark NiS nanoparticles with diameter of 5–20nm were highly deposited on the surface of the flake mpg-$C_3N_4$. The results are in good agreement with the reported ones for the g-$C_3N_4$/NiS hybrid photocatalysts prepared via an in situ template-free ion-exchange process.[52] Clearly, these NiS nanoparticles were directly grown in the voids of mpg-$C_3N_4$ or on the surface of CNTs. The intimate interface contacts between NiS and mpg-$C_3N_4$ (or CNTs) are crucial for the efficient charge transfer. As potential active sites, these NiS nanoparticles can take advantage of the photo-generated electrons on the surface of mpg-$C_3N_4$ or CNTs, thus fundamentally promoted the $H_2$-evolution kinetics.

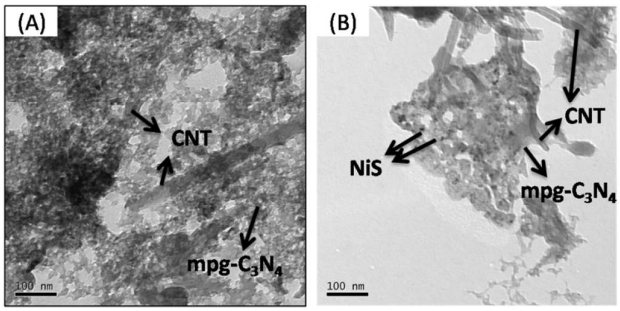

**Figure 2**. TEM images of mpg-$C_3N_4$/CNT (A) and mpg-$C_3N_4$/CNT/1% NiS (B).

To further confirm the formation of the intimate interface contacts in the mpg-$C_3N_4$/CNT/1% NiS ternary hybrid sample, the measured TEM and HRTEM images of the as-prepared mpg-$C_3N_4$/CNT/1% NiS were shown in Figures 3. Obviously, as shown in Figure 3B, the clear lattice fringes of NiS nanoparticles, CNTs and 2D g-$C_3N_4$ nanosheets could be readily identified. It is observed from Figure 3B that the obtained g-$C_3N_4$ crystallites exhibited the lattice spacing of about 0.336 nm, corresponding to the (002) plane of hexagonal g-$C_3N_4$ (JCPDS87-1526).[44] Furthermore, the HRTEM images (Figures 3B and 3C) of mpg-$C_3N_4$/CNT/1% NiS nanocomposite also showed the lattice fringe spacings of 0.33 nm and 0.223 nm, which can be assigned to the (002) plane of CNTs and (211) plane of millerite NiS (JCPDS #02-0693), respectively.[4] The HRTEM results clearly demonstrated the formation of intimate heterostructures in the ternary nanocomposites instead of a simple physical mixture of three components. Thus, the intimate interface contacts of NiS, CNTs and mpg-$C_3N_4$ could be verified, which facilitate the vectorial transfer of charge carriers among three components, therefore greatly enhancing the charge separation and the photocatalytic efficiency.

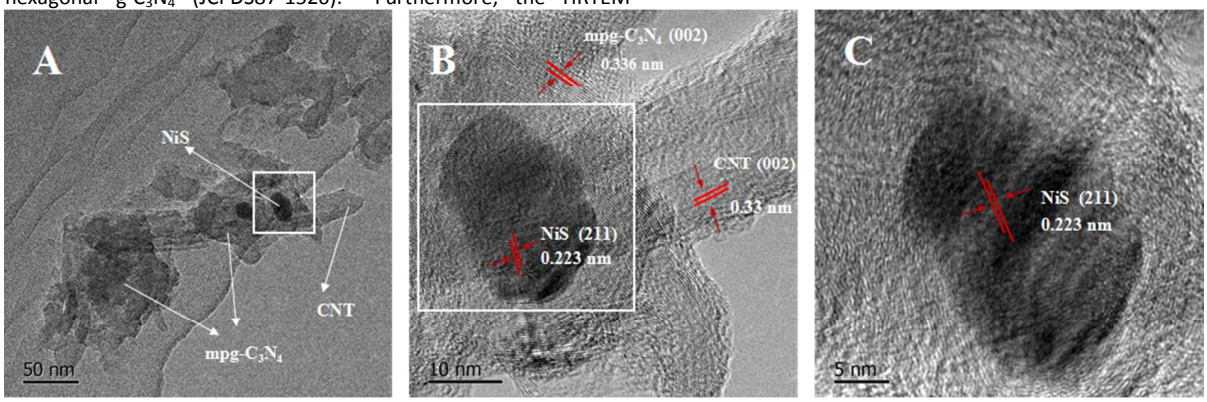


**Figure 3** TEM image of mpg-$C_3N_4$/CNT/1%NiS sample (A) and the corresponding HRTEM images (B) and (C).

### 3.3 XPS analysis

In order to further study the chemical compostion and oxidation state of NiS, CNTs and mpg-$C_3N_4$ in the ternary composites, XPS measurements were also carried out, as depicted in Figure 4A–E. The XPS survey spectrum of the mpg-$C_3N_4$/CNT/1%NiS sample is shown in Figure 4A, obviously indicating the co-existence of the elements C, N, Ni, S and a small amount of O. The corresponding high resolution XPS spectra of C 1s, N 1s, S 2p and Ni 2p of the mpg-$C_3N_4$/CNT/1%NiS sample are shown in Figure 4B–E, respectively. Clearly, the high-resolution C1 s XPS spectra in Figure 4B has two distinct peaks with binding energy of 285.13 and 288.27 eV. The satellite peak at 284.9 eV is ascribed to the $sp^2$ C–C bonds from graphitic carbon adsorbed to the surface and C-C bond from CNTs, indicating the formation of interaction between CNTs and mpg-$C_3N_4$.[59] On the contrary, the main peak located at 288.5 eV could be attributed to the $sp^2$-bonded carbon in the triazine rings (N-C=N), suggesting the major carbon environment in the mpg-$C_3N_4$.[66] As observed in Figure 4C, the main peak of the N 1s spectra at 398.55 eV obviously shows an asymmetrical feature, further confirming the presence of $sp^2$ -bonded N in N-containing aromatic rings (N-C=N) in the mpg-$C_3N_4$. In addition, the obtained S 2p and Ni 2p XPS results (Figures 4D and 4E) can confirm the formation of surface NiS. The binding energies of the weak peak of Ni 2p 3/2 are found at 857.9 eV, which should be attributed to those of Ni $2p_{3/2}$ in NiS.[66] The minor peak of S 2p at 161.1 eV and the major peak at 164.2 eV are close to those of NiS.[52, 66] All above results further confirmed the formation of ternary hybrid composite composed of mpg-$C_3N_4$, CdS and NiS

Journal Name

ARTICLE

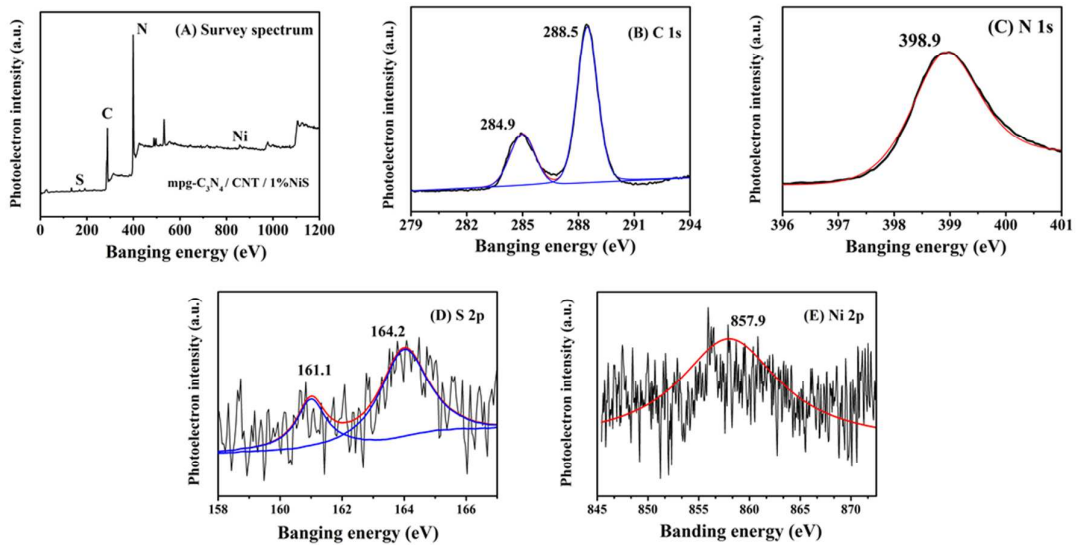


**Figure 4** XPS spectra of mpg-$C_3N_4$/CNT/1%NiS sample; survey spectrum (A), C 1s (B), N 1s (C), S 2p (D), and Ni 2p (E).

### 3.4 Textural properties

The surface areas and porous structures of the mpg-$C_3N_4$/CNT/NiS composite were also measured by nitrogen adsorption–desorption isotherms. Figure 5 shows the whole $N_2$ adsorption–desorption isotherms at 77 K and the corresponding pore size distribution curves. The pore size distribution was obtained from the desorption branch of the isotherms by the BJH method. As can be seen clearly in Figure 5, three studied samples exhibit a typical type-IV adsorption–desorption isotherm with a H3 hysteresis loop according to the IUPAC classification, suggesting the presence of mesoporous structures.[67] It is generally believed that the Type H3 hysteresis loop is associated with capillary condensation taking place in slit-shaped mesopores, which may originate from the aggregates of plate-like mpg-$C_3N_4$ sheets. The corresponding pore size distribution curves further confirm that the all three samples are mesoporous materials with a mean pore diameter in the range of 10–20 nm (inset in Figure 5). The textural parameters of three photocatalysts are summarized in Table 2. As seen from the Table 2, all samples exhibit a mean pore diameter between 2 and 50 nm, indicating their mesoporous structures. Furthermore, the loading of NiS onto mpg-$C_3N_4$/CNT photocatalyst could lead to a significant decrease in the BET specific surface, mean pore diameter and pore volume, which may be due to the formation of NiS nanoparticles in the mesopores of mpg-$C_3N_4$.[68] In addition, it should be noted that the surface area and pore volume of mpg-$C_3N_4$/CNT composite are obviously much smaller than those of pure mpg-$C_3N_4$, which may be due to that the addition of CNTs has a negative influence on the homogeneous copolymerization of cyanamide molecules and the formation of mesopores. These data suggest that the enhancements in the surface areas and pore volume are not the key factors for boosting the photocatalytic activity of mpg-$C_3N_4$/CNT/1% NiS.[69]

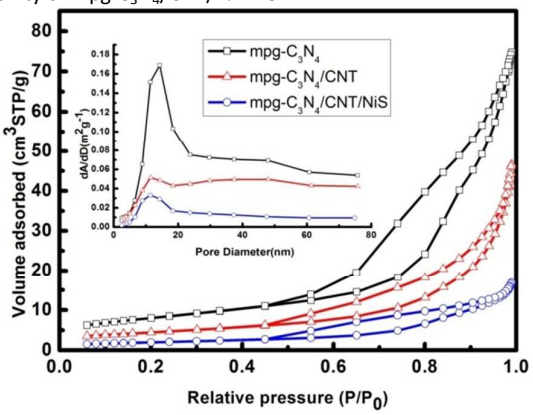


**Figure 5**. $N_2$ adsorption–desorption isotherms and the corresponding pore size distribution curves (inset) of mpg-$C_3N_4$, mpg-$C_3N_4$/CNT and mpg-$C_3N_4$/CNT/1% NiS.

Table 2. Pore structure parameter of mpg-$C_3N_4$, mpg-$C_3N_4$/CNT and mpg-$C_3N_4$/CNT/1% NiS

| Photocatalysts | BET surface area ($m^2g^{-1}$) | Mean pore diameter (nm) | Pore volume \($cm^3g^{-1}$) |
|---|---|---|---|
| mpg-$C_3N_4$ | 28.3953 | 15.36687 | 0.116515 |

| | | | |
|---|---|---|---|
| mpg-$C_3N_4$/CNT | 15.6450 | 16.20376 | 0.072624 |
| Mpg-$C_3N_4$/CNT/1%NiS | 7.0009 | 13.49817 | 0.026325 |

### 3.5 UV-vis absorption spectra

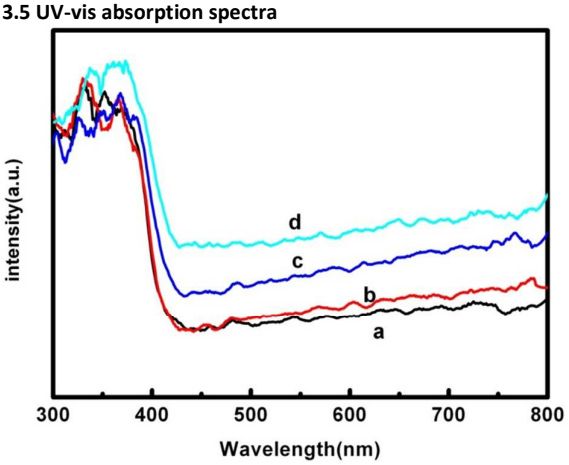


The optical properties of the as-obtained mpg-$C_3N_4$/CNT and mpg-$C_3N_4$/CNT/NiS composite samples were determined by using the UV-vis absorption spectra. The UV-vis diffuse reflection spectra of the mpg-$C_3N_4$/CNT samples with different NiS contents were shown in Figure 6. As observed from Figure 6, it is clear that the spectra of mpg-$C_3N_4$/CNT displays an absorption edge at about 455 nm, corresponding to band gap of 2.72 eV. It is also noted that the introduction of NiS co-catalysts could not lead to a significant shift of the absorption edge, implying that the NiS co-catalysts were only loaded on the surface of mpg-$C_3N_4$/CNT. Furthermore, the absorption intensity in the visible region (over 460 nm) in the mpg-$C_3N_4$/CNT/NiS composite samples is gradually enhanced with increasing the loading content of NiS. Therefore, it is obvious that the introduction of NiS co-catalysts play an additional role in increasing the visible-light absorption of composites, which may be also beneficial for the enhancement of visible-light photocatalytic $H_2$-evolution activities.

**Figure 6**. UV-vis diffuse-reflectance spectra of all the synthesised samples. (a) mpg-$C_3N_4$/CNT, (b) mpg-$C_3N_4$/CNT/0.5% NiS, (c) mpg-$C_3N_4$/CNT/1% NiS, and (d) mpg-$C_3N_4$/CNT/3% NiS.

### 3.6 Photocatalytic activities and stability

The photocatalytic $H_2$-evolution activity of all the samples was evaluated under the condition of visible light (λ>420 nm) and using 10% triethanolamine aqueous solution as a hole sacrficial reagent. No $H_2$ production was detected without photocatalysts or light irradiation, indicating that $H_2$ was generated by the photocatalytic reactions. It was also demonstrated that pure mpg-$C_3N_4$ is inactive for photocatalytic $H_2$ production under the visible light irradiation under current conditions. Figure 7 shows the time profiles and the average rate for the photocatalytic $H_2$ evolution over mpg-$C_3N_4$/CNT with different co-catalysts under visible-light irradiation with simulated solar. It can be noted that the rates of photocatalytic $H_2$ evolution increased with the irradiation time for all samples. As shown in Figure 7B, the average hydrogen evolution rate of mpg-$C_3N_4$/CNT/3%NiS reaches 378 μmol·$g^{-1}h^{-1}$, which is 1.37 and 12.2 times higher than those of the mpg-$C_3N_4$/CNT/3%CoS and mpg-$C_3N_4$/CNT/3%CuS, respectively. Clearly, compared to the CoS and CuS, NiS is the best $H_2$-evolution co-catalysts for the mpg-$C_3N_4$/CNT.

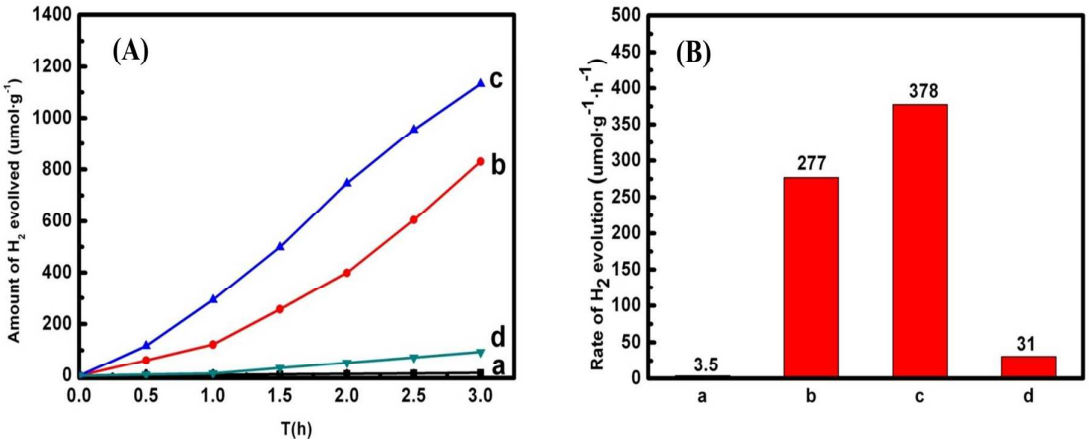


**Figure 7**. (A) Time courses of photocatalytic $H_2$ evolution and (B) the average rate of $H_2$ evolution over the photocatalysts: (a) mpg-$C_3N_4$/CNT，(b) mpg-$C_3N_4$/CNT/3%CoS，(c) mpg-$C_3N_4$/CNT/3%NiS，(d) mpg-$C_3N_4$/CNT/3%CuS. Reaction conditions: catalyst, 0.05 g; 10 mL triethanolamine; 90 mL distilled water; light source, xenon lamp (300 W) with a UV cut-off filter (λ≥420 nm).

To further optimize the $H_2$-evolution rate over the mpg-$C_3N_4$/CNT/NiS composites, the ternary mpg-$C_3N_4$/CNT/NiS hybrids with different loading content of NiS were also fabricated and evaluated. As shown in Figure 8A, all mpg-$C_3N_4$/CNT/NiS composites exhibit better photocatalytic hydrogen evolution performance than the pure mpg-$C_3N_4$/CNT sample. The average hydrogen evolution rates of all mpg-$C_3N_4$/CNT/NiS composites were shown in Figure 8B. Clearly, the mpg-$C_3N_4$/CNT/1% NiS composite exhibits the highest $H_2$-evolution rate of 521 μmol·$g^{-1}h^{-1}$, which is about 148 times as high as that of mpg-$C_3N_4$/CNT. Clearly, the photocatalytic activity increases with increasing NiS loading when it is smaller than 1 wt %. However, when the loading content of NiS is more than 1 wt %, a further increase in NiS content will lead to a significant reduction of

the photocatalytic $H_2$-evolution rate. This decrease can be ascribed to the light scattering and mask effects, which will reduce the light utilization efficiency. In addition, the excess NiS nanoparticles can also act as recombination centers of photo-generated electrons and holes, thus decreasing the photocatalytic activity.

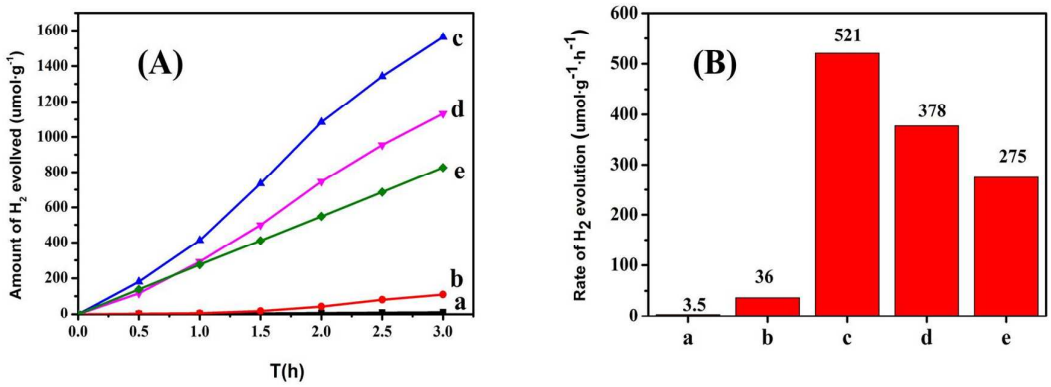


**Figure 8**. (A) Time courses of photocatalytic $H_2$ evolution and (B) the average rates of $H_2$ evolution over the photocatalysts: (a) mpg-$C_3N_4$/CNT, (b)mpg-$C_3N_4$/CNT/0.5% NiS, (c) mpg-$C_3N_4$/CNT/1% NiS, (d) mpg-$C_3N_4$/CNT/3% NiS and (e) 3.0 wt% Pt loaded mpg-$C_3N_4$. Reaction conditions: catalyst, 0.05 g; 10 mL triethanolamine; 90 mL distilled water; light source, xenon lamp (300 W) with a UV cut-off filter (λ≥420 nm)

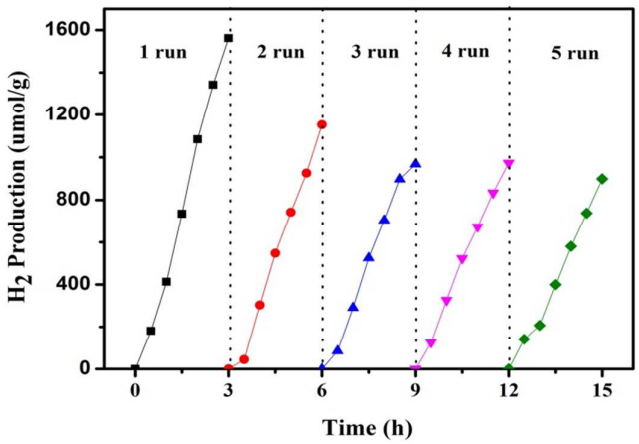


**Figure. 9** Repeated time courses of the photocatalytic $H_2$ production over the mpg-$C_3N_4$/CNT/1%NiS sample. Reaction conditions: catalyst, 0.05 g; 10 mL triethanolamine; 90 mL distilled water; light source, xenon lamp (300 W) with a UV cut-off filter (λ≥420 nm).

The stability and reusability of mpg-$C_3N_4$/CNT/1%NiS for photocatalytic $H_2$ production were evaluated by repeating the photocatalytic experiments under the same conditions for five cycles. The corresponding results are shown in Figure 9. It is found that the obvious deactivation in the photocatalytic hydrogen production activity is detected for the mpg-$C_3N_4$/CNT/1%NiS composite after continuous visible-light irradiation. After three cycles, the amount of generated hydrogen became stable and around 65% that after the first cycle. The decreased activity might be due to the slow break-off of the NiS nanoparticles from mpg-$C_3N_4$ or CNTs surfaces. Similar phenomena can be found in the other g-$C_3N_4$-based photocatalysts loaded by different co-catalysts such as $NiS_2$[54] and $Ag_2S$[47]. Nevertheless, the rate in the fifth cycle is still higher than that of 3 wt% Pt loaded mpg-$C_3N_4$ in the first cycle (as shown in Figure 8). Obviously, the photocatalytic $H_2$-evolution activity over 3 wt% Pt loaded mpg-$C_3N_4$ (275 μmol·$g^{-1}h^{-1}$) in this study is much smaller than the reported value in the literatures (1490 μmol·$g^{-1}h^{-1}$),[38] which may be due to that the different preparation processes for mpg-$C_3N_4$ in our group lead to its smaller surface areas and pore volume, as compared to those reported. However, under the similar condations, the camparasions in our group can clearly reveal that the noble-metal free NiS represents a promising kind of co-catalyst for promoting $H_2$ production under visible light irradiation.

### 3.7 Possible mechanism of the photocatalytic $H_2$ evolution

In order to further understand the role of NiS in charge carrier separation, the photoluminescence (PL) decay spectra of all samples were also investigated. In general, it is accepted that the PL spectra can be used to evaluate the charge migration, transfer and recombination processes in photo-excited semiconductors.[3, 42, 70] As shown in Figure. 10, the PL emission intensity of mpg-$C_3N_4$/CNT/1% NiS composite is the lowest of all, indicating the fastest separation efficiency of charge carriers. This is because that the suitable loading content of NiS cocatalysts, as both active sites and electron transfer channels, can effectively suppress the recombination of the photo generated electrons and holes, thereby lowering the fluorescence intensity. However, when loading content of NiS is too high, the excess NiS co-catalysts can act as recombination centers of photo-generated electrons and holes, thus accelerating their recombination instead of separation. These results show that the synergistic effect between mpg-$C_3N_4$, CNTs and NiS, could promote more efficient separation of photo-generated charge carriers, which plays a crucial role in enhancing the photocatalytic $H_2$-evolution activity.

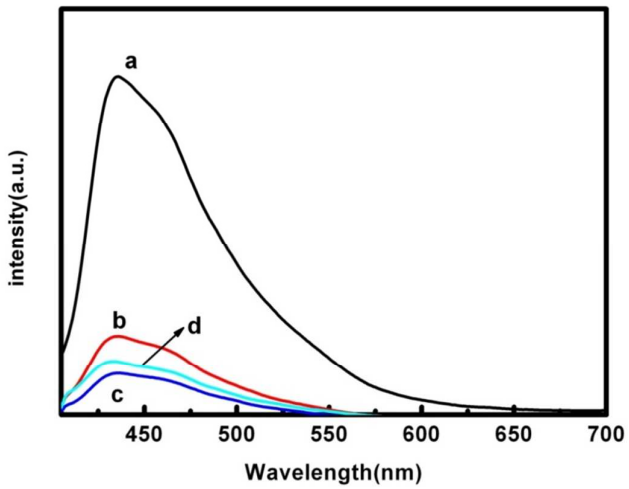


**Figure 10.** Photoluminescence spectra of the photocatalysts: (a) mpg-$C_3N_4$/CNT, (b) mpg-$C_3N_4$/CNT/0.5% NiS, (c) mpg-$C_3N_4$/CNT/1% NiS, and (d) mpg-$C_3N_4$/CNT/3% NiS

To further verify the improved charge separation, photocurrent responses were also recorded. It is known that the transient photocurrent responses of a given photocatalyst may strongly depend on the charge collection and separation efficiency of the photo-generated electron-hole pairs.[16, 42] The transient photocurrent responses of mpg-$C_3N_4$/CNT and mpg-$C_3N_4$/CNT/1%NiS samples were measured in the light on–off process. Figure 11 shows the PEC I-t curves of mpg-$C_3N_4$/CNT and mpg-$C_3N_4$/CNT/1% NiS electrodes under intermittent visible light irradiation (>420 nm) at a bias potential of 0.6 V. All of the samples exhibited prompt and reproducible photocurrent responses on each illumination, while the photocurrent value will be quickly decreased to zero once the light turns off, revealing that photocurrent was reproducible. Clearly, the photocurrent of mpg-$C_3N_4$/CNT/1% NiS sample is much higher than that of mpg-$C_3N_4$/CNT sample, further confirming the more efficient interfacial mobility and separation of photo-generated electron-hole pairs for the mpg-$C_3N_4$/CNT/1% NiS composite sample.

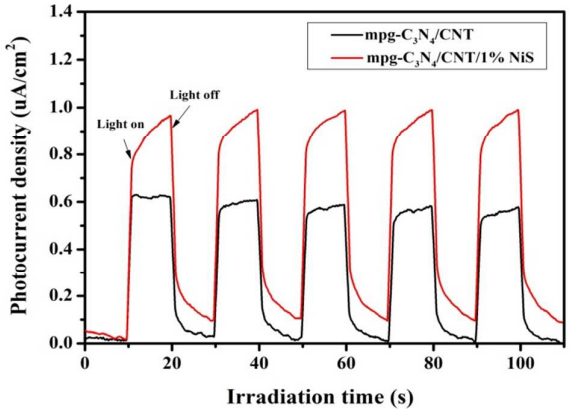


**Figure 11.** The photoelectrochemical (PEC) I-t curves of mpg-$C_3N_4$/CNT and mpg-$C_3N_4$/CNT/1% NiS.

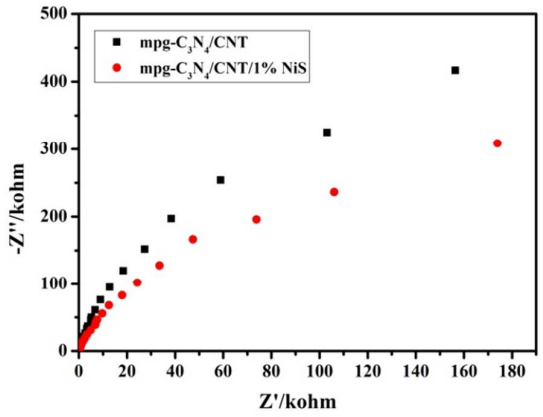


**Figure 12** Nyquist plots of electrochemical impedance spectroscopy with mpg-$C_3N_4$/CNT and mpg-$C_3N_4$/CNT/1% NiS

The electrochemical impedance spectroscopy (EIS, presented as Nyquist plots) has been also investigated to provide sufficient evidence for the interfacial charge transfer resistance and separation efficiency. Generally, it is believed that the smaller arc radius on the EIS Nyquist plot represents a more effective separation of photo-generated electron–hole pairs and a higher efficiency of charge immigration across the electrode/electrolyte interface.[42] Figure 12 shows the EIS Nyquist plots of mpg-$C_3N_4$/CNT and mpg-$C_3N_4$/CNT/1%NiS composits. As shown in Figure 12, it is observed that the Nyquist plots diameter of mpg-$C_3N_4$/CNT/1%NiS is much smaller than that of mpg-$C_3N_4$/CNT, indicating the lower resistance and the faster interfacial charge transfer. The results are in good accordance with the photocatalytic-activity measurements, PL and transient photocurrent results. Therefore, it can be concluded that the faster interfacial transfer and separation of photo-generated charges is an important reason for the enhanced photocatalytic $H_2$-evolution activities of mpg-$C_3N_4$/CNT/1%NiS composite.

On the basis of all the above results, a possible mechanism of the photocatalytic $H_2$ evolution and charge transfer over the mpg-$C_3N_4$/CNT/NiS under visible-light irradiation can be proposed. As shown in Scheme 1, the mpg-$C_3N_4$ could be excited by visible light ($\lambda \geq 420$ nm) and produce the photo-generated electron-hole pairs due to its narrower band gap. It is known that the conduction band (CB) position of mpg-$C_3N_4$ is much more negative than the work function (4.3 eV) for CNTs.[4] Consequently, once the Schottky-type junction between mpg-$C_3N_4$ and conductive CNTs is constructed, the effective charge separation for photo-excited electrons from mpg-$C_3N_4$ to the conducting network of CNTs could be achieved. Therefore, the photo-induced electrons in the CB of mpg-$C_3N_4$ and on the surface of CNTs could effectively drive the photocatalytic $H_2$-evolution on the NiS co-catalysts as active sites, respectively. Meanwhile, the holes on the valence band of mpg-$C_3N_4$ can be directly consumed by the surface reaction of sacrificial reagent oxidation (TEOA) under visible light irradiation. As a result, effectively promoted separation of photo generated electron-hole pairs and enhanced $H_2$-evolution kinetics could be achieved, thus leading to the significant enhancement of the photocatalytic $H_2$

evolution activity over the NiS co-catalysts modified metal-free mpg-$C_3N_4$/CNTs nanocomposites.

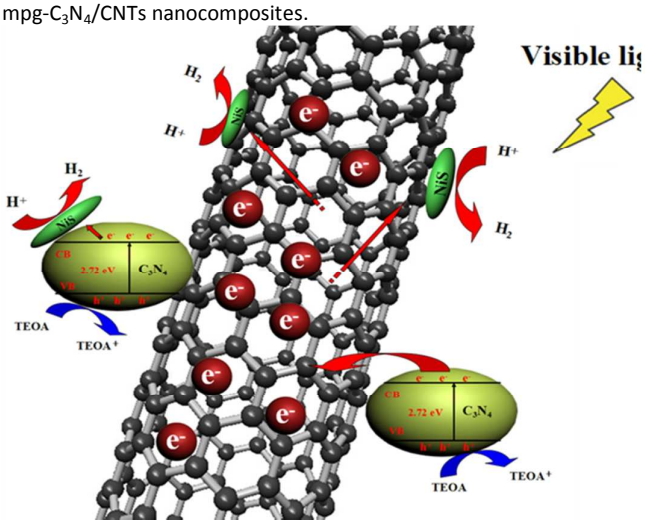


**Scheme 1** Proposed photocatalytic $H_2$-production and charge transfer mechanisms in the mpg-$C_3N_4$/CNT/NiS composite under visible light irradiation.

## Conclusions

In conclusion, we have demonstrated that mpg-$C_3N_4$/CNT/NiS composite was synthesized by a two-step strategy of sol-gel method (for the loading of CNTs) and precipitation process (for the loading of NiS), respectively. The results showed that the mpg-$C_3N_4$/CNT/1%NiS nanocomposite exhibits the best photocatalytic activity with a $H_2$-evolution of about 521 $\mu mol \cdot g^{-1}h^{-1}$ under visible light ($\lambda$>420 nm), which is almost 148 times higher than that of pure mpg-$C_3N_4$/CNT sample. It is believed that the NiS co-catalysts, can effectively suppress the recombination of the photo-generated electrons and holes and photocatalytic $H_2$-evolution kinetics. In this work, the improved photocatalytic $H_2$-evolution activity of $C_3N_4$-based materials could be achieved via the co-loading noble-metal free NiS and carbonaceous nanomaterials, which may provide a promising class of photocatalyst candidates for photocatalytic $H_2$-production and solar energy conversion.

## Acknowledgements

The work was supported by the National Natural Science Foundation of China (20906034, 20963002, 21173088 and 21207041). This work was also partly supported by the State Key Laboratory of Catalysis cooperation project (N-08-08) and the State Key Laboratory of Advanced Technology for Material Synthesis and Processing (Wuhan University of Technology) (2015-KF-7).

## Notes and references

‡Footnotes relating to the main text should appear here. These might include comments relevant to but not central to the matter under discussion, limited experimental and spectral data, and crystallographic data.

§
§§
etc.

1. J. A. Turner, *Science*, 2004, **305**, 972-974.
2. J. Yuan, J. Wen, Q. Gao, S. Chen, J. Li, X. Li and Y. Fang, *Dalton Trans.*, 2015, **44**, 1680-1689.
3. X. Zhou, Q. Gao, X. Li, Y. Liu, S. Zhang, Y. Fang and J. Li, *J. Mater. Chem. A*, 2015, **3**, 10999-11005.
4. X. Zhou, X. Li, Q. Gao, J. Yuan, J. Wen, Y. Fang, W. Liu, S. Zhang and Y. Liu, *Catal. Sci. Technol.*, 2015, **5**, 2798-2806.
5. F. A and H. K, *Nature*, 1972, **238**, 37-38.
6. X. Chen, S. Shen, L. Guo and S. S. Mao, *Chem. Rev.*, 2010, **110**, 6503-6570.
7. X. Li, J. Yu, J. Low, Y. Fang, J. Xiao and X. Chen, *J. Mater. Chem. A*, 2015, **3**, 2485-2534.
8. X. Wang, K. Maeda, A. Thomas, K. Takanabe, G. Xin, J. M. Carlsson and M. Antonietti, *Nat. Mater.*, 2009, **8**, 76 - 80.
9. Z. Zhao, Y. Sun and F. Dong, *Nanoscale*, 2014, **7**, 15-37.
10. J. Yu, S. Wang, J. Low and W. Xiao, *Phys. Chem. Chem. Phys.*, 2013, **15**, 16883-16890.
11. S. Cao, J. Low, J. Yu and M. Jaroniec, *Adv. Mater.*, 2015, **27**, 2150-2176.
12. S. Cao and J. Yu, *J. Phys. Chem. Lett.*, 2014, **5**, 2101-2107.
13. J. Liu, Y. Liu, N. Liu, Y. Han, X. Zhang, H. Huang, Y. Lifshitz, S.-T. Lee, J. Zhong and Z. Kang, *Science*, 2015, **347**, 970-974.
14. Q. Xiang, J. Yu and M. Jaroniec, *J. Phys. Chem. C*, 2011, **115**, 7355-7363.
15. R. Kuriki, K. Sekizawa, O. Ishitani and K. Maeda, *Angew. Chem. Int. Edit.*, 2015, **54**, 2406-2409.
16. K. Wang, Q. Li, B. Liu, B. Cheng, W. Ho and J. Yu, *Applied Catalysis B: Environmental*, 2015, **176–177**, 44-52.
17. J. Mao, T. Peng, X. Zhang, K. Li, L. Ye and L. Zan, *Catal. Sci. Technol.*, 2013, **3**, 1253-1260.
18. J. Yu, K. Wang, W. Xiao and B. Cheng, *Phys. Chem. Chem. Phys.*, 2014, **16**, 11492-11501.
19. L. Yuan and Y.-J. Xu, *Appl. Surf. Sci.*, 2015, **342**, 154-167.
20. X. Li, J. Wen, J. Low, Y. Fang and J. Yu, *Science China Materials*, 2014, **57**, 70–100.
21. F. Su, S. C. Mathew, G. Lipner, X. Fu, M. Antonietti, S. Blechert and X. Wang, *J. Am. Chem. Soc.*, 2010, **132**, 16299-16301.
22. X. Chen, J. Zhang, X. Fu, M. Antonietti and X. Wang, *J. Am. Chem. Soc.*, 2009, **131**, 11658-11659.
23. J. Xu, T. J. K. Brenner, L. Chabanne, D. Neher, M. Antonietti and M. Shalom, *J. Am. Chem. Soc.*, 2014, **136**, 13486-13489.
24. J. Xu, G. Wang, J. Fan, B. Liu, S. Cao and J. Yu, *J. Power. Sources.*, 2015, **274**, 77-84.
25. J. S. Zhang, X. F. Chen, K. Takanabe, K. Maeda, K. Domen, J. D. Epping, X. Z. Fu, M. Antonietti and X. C. Wang, *Angew. Chem. Int. Edit.*, 2010, **49**, 441-444.
26. J. Zhang, J. Sun, K. Maeda, K. Domen, P. Liu, M. Antonietti, X. Fu and X. Wang, *Energy Environ. Sci.*, 2011, **4**, 675-678.
27. Y. Zhang, T. Mori, J. Ye and M. Antonietti, *J. Am. Chem. Soc.*, 2010, **132**, 6294-6295.
28. X. Bai, L. Wang, R. Zong and Y. Zhu, *J. Phys. Chem. C*, 2013, **117**, 9952-9961.
29. J. Xu, L. Zhang, R. Shi and Y. Zhu, *J. Mater. Chem. A*, 2013, **1**, 14766-14772.
30. S. Yang, Y. Gong, J. Zhang, L. Zhan, L. Ma, Z. Fang, R. Vajtai, X. Wang and P. M. Ajayan, *Adv. Mater.*, 2013, **25**, 2452-

2456.
31. J. Sun, J. Zhang, M. Zhang, M. Antonietti, X. Fu and X. Wang, *Nat. Commun.*, 2012, **3**, 1139.
32. Y. Zhou, L. Zhang, J. Liu, X. Fan, B. Wang, M. Wang, W. Ren, J. Wang, M. Li and J. Shi, *J. Mater. Chem. A*, 2015, **3**, 3862-3867.
33. G. Zhang, M. Zhang, X. Ye, X. Qiu, S. Lin and X. Wang, *Adv. Mater.*, 2014, **26**, 805-809.
34. S. Hu, L. Ma, J. You, F. Li, Z. Fan, G. Lu, D. Liu and J. Gui, *Appl. Surf. Sci.*, 2014, **311**, 164-171.
35. J. Yu, S. Wang, B. Cheng, Z. Lin and F. Huang, *Catal. Sci. Technol.*, 2013, **3**, 1782-1789.
36. X. Zhou, Z. Luo, P. Tao, B. Jin, Z. Wu and Y. Huang, *Mater. Chem. Phys.*, 2014, **143**, 1462-1468.
37. Q. Gu, Y. Liao, L. Yin, J. Long, X. Wang and C. Xue, *Appl. Catal. B-Environ.*, 2015, **165**, 503-510.
38. X. Wang, K. Maeda, X. Chen, K. Takanabe, K. Domen, Y. Hou, X. Fu and M. Antonietti, *J. Am. Chem. Soc.*, 2009, **131**, 1680-1681.
39. S. Min and G. Lu, *J. Phys. Chem. C*, 2012, **116**, 19644-19652.
40. J. Xu, Y. Li, S. Peng, G. Lu and S. Li, *Phys. Chem. Chem. Phys.*, 2013, **15**, 7657-7665.
41. Y. Wang, J. Hong, W. Zhang and R. Xu, *Catal. Sci. Technol.*, 2013, **3**, 1703-1711.
42. D. Chen, K. Wang, W. Hong, R. Zong, W. Yao and Y. Zhu, *Appl. Catal. B-Environ.*, 2015, **166**, 366-373.
43. S.-W. Cao, Y.-P. Yuan, J. Fang, M. M. Shahjamali, F. Y. C. Boey, J. Barber, S. C. J. Loo and C. Xue, *Int. J. Hydrogen. Energ.*, 2013, **38**, 1258-1266.
44. L. Ge, F. Zuo, J. Liu, Q. Ma, C. Wang, D. Sun, L. Bartels and P. Feng, *J. Phys. Chem. C*, 2012, **116**, 13708-13714.
45. J. Zhang, Y. Wang, J. Jin, J. Zhang, Z. Lin, F. Huang and J. Yu, *Acs Appl. Mater. Inter.*, 2013, **5**, 10317-10324.
46. J. Hong, X. Xia, Y. Wang and R. Xu, *J. Mater. Chem.*, 2012, **22**, 15006-15012.
47. D. Jiang, L. Chen, J. Xie and M. Chen, *Dalton Trans.*, 2014, **43**, 4878-4885.
48. L. Ge, C. Han, X. Xiao and L. Guo, *Int. J. Hydrogen. Energ.*, 2013, **38**, 6960-6969.
49. Y. Hou, A. B. Laursen, J. Zhang, G. Zhang, Y. Zhu, X. Wang, S. Dahl and I. Chorkendorff, *Angew. Chem. Int. Edit.*, 2013, **52**, 3621-3625.
50. Y. Hou, Y. Zhu, Y. Xu and X. Wang, *Appl. Catal. B-Environ.*, 2014, **156**, 122-127.
51. S. Samanta, S. Martha and K. Parida, *Chemcatchem*, 2014, **6**, 1453-1462.
52. Z. Chen, P. Sun, B. Fan, Z. Zhang and X. Fang, *J. Phys. Chem. C*, 2014, **118**, 7801-7807.
53. J. Hong, Y. Wang, Y. Wang, W. Zhang and R. Xu, *Chemsuschem*, 2013, **6**, 2200-2200.
54. L. Yin, Y.-P. Yuan, S.-W. Cao, Z. Zhang and C. Xue, *Rsc. Adv.*, 2014, **4**, 6127-6132.
55. Y.-N. Zhang, X.-H. Li, Y.-Y. Cai, L.-H. Gong, K.-X. Wang and J.-S. Chen, *Rsc. Adv.*, 2014, **4**, 60873-60877.
56. Y. Zhu, Y. Xu, Y. Hou, Z. Ding and X. Wang, *Int. J. Hydrogen. Energ.*, 2014, **39**, 11873-11879.
57. Y. Xu and R. Xu, *Appl. Surf. Sci.*, 2015, **351**, 779-793.
58. J. Ran, J. Zhang, J. Yu, M. Jaroniec and S. Z. Qiao, *Chem. Soc. Rev.*, 2014, **43**, 7787-7812.
59. L. Ge and C. Han, *Appl. Catal. B-Environ.*, 2012, **117**, 268-274.
60. A. Suryawanshi, P. Dhanasekaran, D. Mhamane, S. Kelkar, S. Patil, N. Gupta and S. Ogale, *Int. J. Hydrogen. Energ.*, 2012, **37**, 9584-9589.
61. Y. Chen, J. Li, Z. Hong, B. Shen, B. Lin and B. Gao, *Phys. Chem. Chem. Phys.*, 2014, **16**, 8106-8113.
62. J. Yu, B. Yang and B. Cheng, *Nanoscale*, 2012, **4**, 2670-2677.
63. Q. Li, X. Li, S. Wageh, A. A. Al-Ghamdi and J. Yu, *Adv. Energy Mater.*, 2015, **5**, 1500010.
64. Q. J. Xiang, J. G. Yu and M. Jaroniec, *Chem. Soc. Rev.*, 2012, **41**, 782-796.
65. X. Zhou, X. Li, Q. Gao, J. Yuan, J. Wen, Y. Fang, W. Liu, S. Zhang and Y. Liu, *Catal. Sci. Technol.*, 2015, **5**, 2798-2806.
66. J. Yuan, J. Wen, Y. Zhong, X. Li, Y. Fang, S. Zhang and W. Liu, *J. Mater. Chem. A*, 2015, DOI: 10.1039/C5TA04573H.
67. K. Sing, D. Everett, R. Haul, L. Moscou, R. Pierotti, J. Rouquerol and T. Siemieniewska, *Pure Appl. Chem*, 1985, **57**, 603-619.
68. X. Li, H. Li, S. Huo and Z. Li, *Kinet. Catal+.* 2010, **51**, 754-761.
69. X. Li, H. Liu, D. Luo, J. Li, Y. Huang, H. Li, Y. Fang, Y. Xu and L. Zhu, *Chem. Eng. J.*, 2012, **180**, 151-158.
70. J. Yuan, J. Wen, Q. Gao, S. Chen, J. Li, X. Li and Y. Fang, *Dalton Trans.*, 2015, **44**, 1680-1689.

Graphical Abstract

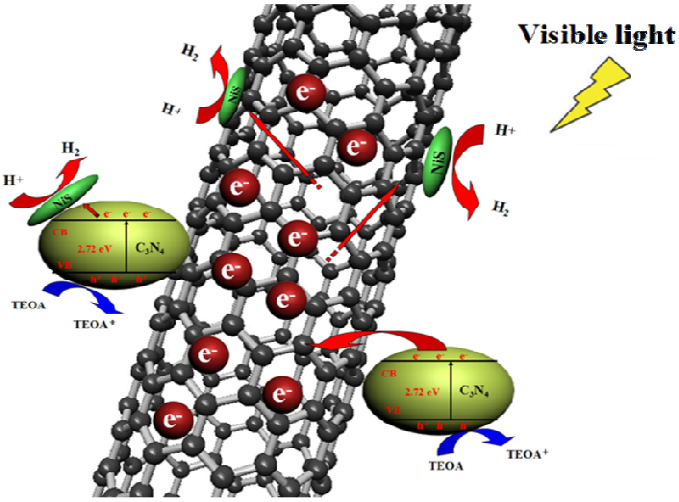


NiS modified mpg-$C_3N_4$/CNTs photocatalysts exhibit significantly enhanced photocatalytic $H_2$-evolution activities under visible light irradiation.